Photochemical & Photobiological Sciences (2023) 22:2759–2768
https://doi.org/10.1007/s43630-023-00484-4

ORIGINAL PAPERS

Ni(II)-doped $CuWO_4$ photoanodes with enhanced photoelectrocatalytic activity

Chiara Nomellini[1] · Annalisa Polo[1] · Ivan Grigioni[1] · Gianluigi Marra[2] · Maria Vittoria Dozzi[1] · Elena Selli[1]

Received: 30 May 2023 / Accepted: 18 September 2023 / Published online: 13 October 2023

Abstract

$CuWO_4$ has emerged in the last years as a ternary metal oxide material for photoanodes application in photoelectrochemical cells, thanks to its relatively narrow band gap, high stability and selectivity toward the oxygen evolution reaction, though largely limited by its poor charge separation efficiency. Aiming at overcoming this limitation, we investigate here the effects that Cu(II) ion substitution has on the photoelectrocatalytic (PEC) performance of copper tungstate. Optically transparent $CuWO_4$ thin-film photoanodes, prepared via spin coating and containing different amounts of Ni(II) ions, were fully characterized via UV–Vis spectroscopy, XRD and SEM analyses, and their PEC performance was tested via linear sweep voltammetry, incident photon to current efficiency and internal quantum efficiency analyses. From tests performed in the presence of a hole scavenger-containing electrolyte, the charge injection and separation efficiencies of the electrodes were also calculated. Pure-phase crystalline and/or heterojunction materials were obtained with higher PEC performance compared to pure $CuWO_4$, mainly due to a significantly enhanced charge separation efficiency in the bulk of the material.

Graphic abstract

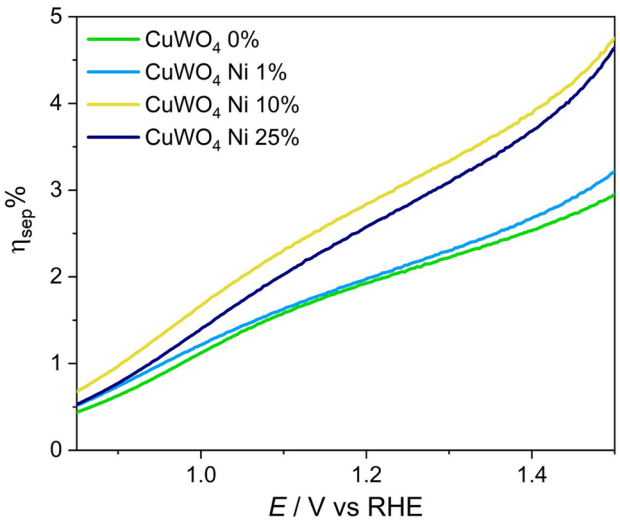

Keywords Copper tungstate · Photoanode · Nickel doping · Photoactivity enhancement · Charge separation efficiency

✉ Elena Selli
elena.selli@unimi.it

[1] Dipartimento di Chimica, Università degli Studi di Milano, Via Golgi 19, 20133 Milan, Italy

[2] ENI S.p.A. Novara Laboratories (NOLAB), Renewable New Energies and Material Science Research Center (DE-R&D), Via G. Fauser 4, 28100 Novara, Italy

1 Introduction

Finding new, sustainable energy sources is the most efficient and effective solution to the energy and environmental crisis that emerged in the last decades [1–3]. One of the most

encouraging routes consists in exploiting the large amount of solar energy that every day strikes the Earth's surface [4, 5]. Large efforts have been focused on how to capture, convert and store this type of energy in a cost-effective fashion [6, 7]. Photocatalytic water splitting has recently attracted increasing attention, because it allows to produce hydrogen, i.e., to convert solar energy into a storable fuel [8, 9], employing semiconductors as photocatalysts. The big challenge is now to identify efficient, stable and low-cost photoactive materials for this application [10, 11].

Interest has been recently drawn on ternary metal oxides as efficient photoanodes for the water oxidation reaction, since in these semiconductors metal-based d orbitals and O(2p) orbitals co-contribute to the valence band maxima, allowing to fine-tune the position of the valence and conduction bands, as well as the band gap energy [12–14]. At present, $BiVO_4$ is the most studied and best-performing ternary oxide [15–17], while other multicomponent materials such as $ZnFe_2O_4$ and $CuWO_4$ are emerging [18–22].

$CuWO_4$ is a n-type semiconductor, which is a promising candidate to work as a photoanode in a photoelectrocatalytic (PEC) cell, due to its relatively small ~ 2.3 eV band gap, its stability under the highly oxidizing conditions of the O_2 evolution reaction and its high selectivity toward oxygen evolution [23, 24]. This material could potentially mitigate some issues frequently encountered in most semiconductor oxides, such as the limited stability in neutral or basic aqueous solutions, being stable and well performing under the highly oxidizing conditions of PEC oxygen evolution, up to pH 9 [25].

Bartlett et al. demonstrated through electrochemical impedance spectroscopy that the onset of photocurrent in $CuWO_4$ thin-film electrodes is dictated by the presence of a midgap state, likely composed of Cu(3d) orbitals [26]. Recently, these midgap states have been energetically located at 0.51 V_{RHE} due to the presence of Fermi level pinning in Mott–Schottky plots [27]. The holes photogenerated in the valence band can either directly oxidize water or become trapped in the intra-band gap states and then react with water molecules. However, these midgap states may also favor detrimental charge recombination processes, limiting the mobility of photogenerated charge carriers [28, 29]. Building heterojunctions [30–32], tuning surface defectivity [13, 21], or coating $CuWO_4$ with cocatalysts [33, 34] have been attempted to overcome these intrinsic limitations.

Successful doping of $CuWO_4$ has been attained by substituting copper with Fe(III) ions [35], resulting in Fe(III)-doped photoanodes with increased photocurrent and separation efficiency. However, very limited studies have focused on identifying alternative elements to substitute Cu^{2+} in the copper tungstate crystalline structure [36]. More attention was drawn on substituting Mo^{6+} for W^{6+} ions, which led to visible light-sensitized photoanodes characterized by an extended band gap energy [37, 38], and on preparing morphology-controlled photoanodes with increased surface area [39, 40].

In the present work we explore the effects of Ni^{2+} for Cu^{2+} substitution in copper tungstate, by systematically investigating for the first time the optical, structural and PEC properties of $CuWO_4$ thin-film photoanodes with different contents of Ni(II) ions. Nickel(II) was chosen as dopant species because Ni^{2+} has an ionic radius similar to that of Cu^{2+}, which would favor the substitution of copper ions within the $CuWO_4$ lattice. Furthermore, very recent studies have focused on the $CuWO_4/NiWO_4$ heterojunction [41] and on nickel-containing copper tungstate coupled with other materials for different applications [42–44] and evidenced an increased PEC performance attained upon partial Ni^{2+} for Cu^{2+} substitution in $CuWO_4$, though the origin of such an effect was not investigated. Our results evidence an increased photocurrent generated by Ni(II)-doped photoanodes compared to pure $CuWO_4$, with the 10% Ni(II)-doped material being best performing, mainly due to a 50% increase in charge separation efficiency.

2 Experimental section

2.1 Materials

The following chemicals were purchased from Sigma-Aldrich and were used as supplied: copper(II) nitrate trihydrate (99%), ammonium metatungstate hydrate (99%), nickel(II) nitrate hexahydrate (99%), citric acid (99%), boric acid (99%), potassium hydroxide (85%) and ethanol (99%).

2.2 Photoelectrodes preparation

To obtain 1 mL of 0.5 M $CuWO_4$ precursor solution, 0.2703 g of citric acid, 0.1220 g of $Cu(NO_3)_2{\cdot}3H_2O$ and 0.1239 g of $(NH_4)_6H_2W_{12}O_{40}{\cdot}xH_2O$ were added to 0.77 mL of a 2:1 ethanol/water solution. The solution was then stirred for about 10 min to fully dissolve the powders, thus obtaining a blue paste. This solution was later deposited on a 2 mm-thick fluorine-doped tin oxide (FTO) glass (Kintec Glass, 7-Ω/sq) by spin coating at 4000 rpm for 30 s. Prior to deposition, the FTO glass was cleaned by 30 min-long sonication in a soap solution, then washed carefully, sonicated in ethanol for 30 min and finally dried in air. A 15-min UV-cleaner ozone treatment was performed onto the clean glass slices to increase the hydrophilicity of the FTO surface. Finally, the slices were soaked in isopropanol for a few seconds right before the deposition, to reduce the light scattering of the prepared films in the long-wavelength spectral region. The so-prepared copper

tungstate electrodes were then dried in air on a hotplate at 250 °C for 10 min and later annealed at 550 °C for 1 h.

Ni(II)-doped $CuWO_4$ photoanodes were prepared following the synthesis described in a previous work [35]. To dope only the copper site, 50 µL of equimolar W(VI) and Ni(II) precursor solutions were added to 1 mL of the previously prepared $CuWO_4$ paste, attaining $Cu_{1-x}Ni_xWO_4$ samples. The Ni(II)-containing solutions were then deposited onto FTO and successively annealed as previously described. Three different doping percentages were investigated, corresponding to a Ni(II) content of 1, 10 and 25% with respect to Cu(II) ions. The so obtained electrodes are labeled as $CuWO_4$ Ni X%, with X referring to the Ni(II) content, while the pure $CuWO_4$ electrode is labeled $CuWO_4$ 0%.

2.3 Optical, morphological and photoelectrochemical characterization

UV–visible absorption spectra were recorded in the transmission mode using a Jasco V-670 spectrophotometer. Structural information on the electrodes was obtained through X-ray diffraction (XRD) analyses, employing an X'Pert PRO PANalytical diffractometer equipped with a Cu sealed tube. The morphologies of pure $CuWO_4$ and of $CuWO_4$–Ni(II) 25% were investigated by means of top-view images acquired using a ultrahigh resolution Jeol JSM 7600f Schottky Field Emission Scanning Electron Microscope (SEM) with 5 keV energy beam.

Linear sweep voltammetry (LSV) measurements were performed using a three-electrode glass cell with two quartz windows. The FTO/$CuWO_4$ photoanodes were employed as working electrodes, while an Ag/AgCl (3.0 M NaCl) electrode and a platinum gauze were used as reference and counter electrode, respectively; an Autolab PGSTAT 12 was employed as potentiostat. The light source was an Oriel, Model 81,172 Solar Simulator equipped with an AM 1.5G filter (1 Sun). The incident light intensity was fixed at 100 mW cm^{-2} measured by means of a Thorlabs PM200 power meter equipped with an S130VC power head with Si detector.

The prepared photoanodes were tested under both backside (through the FTO glass) and front-side (through the deposited film) irradiation in a 0.1 M H_3BO_3 electrolyte solution, buffered at pH 9 by the addition of KOH (KBi). LSV tests were performed also in the presence of $NaNO_2$, as hole scavenger. Previous work demonstrated that a 0.1 M $NaNO_2$ solution in 0.1 M KBi at pH 9, displaying a negligible dark current with increasing photocurrent density, is the best-suited hole scavenger-containing electrolyte for this type of materials among numerous alternatives (Na_2SO_3, H_2O_2, NH_3) [37]. The potential vs. Ag/AgCl was converted to the RHE scale using the following equation:

$$E_{RHE} = E_{AgCl} + 0.059\ pH + E^{\circ}_{AgCl},\ \text{with } E^{\circ}_{AgCl}(3.0\ M\ NaCl) = 0.210\ V \text{ at } 25\ ^{\circ}C.$$

The incident photon to current efficiency (IPCE) was measured in the above-described three-electrode cell, using a 300 W Lot-Oriel Xe lamp as light source, equipped with a Lot-Oriel Omni-λ 150 monochromator and a Thorlabs SC10 automatic shutter. An external bias of 1.23 V vs. RHE was applied in all measurements; the photocurrent was recorded with a 10 nm step within the 300–550 nm wavelength range. IPCE values at each wavelength λ were calculated using the following equation:

$$\text{IPCE\%} = \frac{1240 \times J}{P_{\lambda} \times \lambda} \times 100, \quad (1)$$

where J is the photocurrent density (mA cm^{-2}) and P_{λ} (mW cm^{-2}) is the power of the monochromatic light at a specific wavelength λ (nm).

Since the so determined IPCE values do not take into account losses of incident photons that are reflected or transmitted, the inherent photoefficiency of a material can better be evaluated referring to the number of photons effectively absorbed by the photoactive material, i.e., in terms of internal quantum efficiency (IQE), defined as:

$$\text{IQE\%} = \frac{\text{IPCE\%}}{\eta_{e^-/h^+}}, \quad (2)$$

where η_{e^-/h^+} is the absorptance, i.e., the fraction of electron–hole pairs generated per incident photon.

3 Results and discussion

3.1 Photoanodes characterization

The absorption spectra of pure and Ni(II)-doped $CuWO_4$ photoanodes are reported in Fig. 1a. The absorption profile of pure $CuWO_4$ (i.e., $CuWO_4$ 0%) indicates the attainment of an indirect band gap material characterized by a low absorption coefficient, with an absorption onset at *ca.* 530 nm, consistent with the ~ 2.3 eV band gap reported for this material [20]. The spectra of the doped electrodes are similar in shape to that of the pure material, which suggests that Ni(II) doping in the investigated percent range does not significantly influence the band gap energy of copper tungstate, though the presence of interference fringes in the absorption spectra, consequent to the very low thickness of the absorbing layer, does not allow to appreciate small differences in the absorption onset of the different materials. Doped samples, however, exhibit slightly lower absorption compared to pure

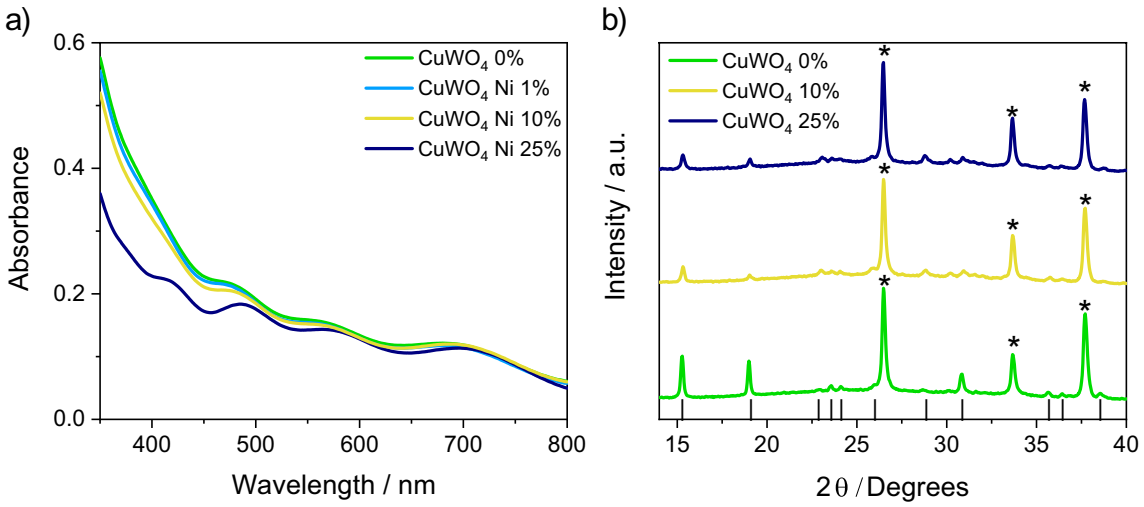

Fig. 1 **a** Absorption spectra of pure and of all Ni(II)-doped $CuWO_4$ electrodes; **b** X-ray diffraction patterns of pure, 10% and 25% Ni(II)-doped $CuWO_4$; the peaks indicated with an asterisk are ascribed to FTO

$CuWO_4$, seemingly decreasing with increasing dopant content. This is in line with the evidence of a much lower Kubelka–Munk function vs. wavelength for pure $NiWO_4$ with respect to pure $CuWO_4$ [45], though the two curves have very similar shape.

Figure 1b reports the XRD patterns of pure $CuWO_4$ and of the two films containing the largest Ni(II) amounts, which indicate that a pure-phase, crystalline material was obtained, even for a relatively high nickel content. In fact, all photoanodes display the diffraction peaks ascribable to the triclinic wolframite structure reported for pure $CuWO_4$ electrodes in previous studies [23, 24]. Thus, no evidence is provided that Ni(II) doping up to 25% affects the crystalline structure of $CuWO_4$, or leads to the formation of impurity phases. However, Ni(II) doping altered the relative intensity of the diffraction peaks. In fact, in the diffraction pattern of $CuWO_4$ 0%, the diffraction peaks at 15.3°, 19.0° and 30.8°, corresponding to the (010), (100) and (111) crystal faces of $CuWO_4$, respectively [46, 47], are more intense than in the diffraction pattern of nickel-containing electrodes. A recent experimental study, supported by DFT calculations, evidenced that $CuWO_4$ films with a high exposure of (100) facets are characterized by a promoted charge transport and a favored oxygen evolution reaction kinetics [47].

On the other hand, the presence of both the $CuWO_4$ triclinic phase and the $NiWO_4$ monoclinic phase have been very recently detected in powder form $Cu_{0.8}Ni_{0.2}WO_4$ obtained through a hydrothermal synthesis [44], exhibiting a much better resolved XRD spectrum than those recorded with our thin-film materials. Furthermore, distinct interfaces between $CuWO_4$ and $NiWO_4$ nanocrystals appear in the HRTEM images of the $Cu_{0.8}Ni_{0.2}WO_4$ material, suggesting that its nanoparticles were composed of $CuWO_4$ and $NiWO_4$ nanocrystals. Thus, a similar composition cannot be excluded for our $CuWO_4$–Ni(II) 25% sample, with high-level Ni doping resulting in a heterojunction system formation, rather than in Ni^{2+} for Cu^{2+} lattice substitution.

The different surface morphology of the $CuWO_4$ and $CuWO_4$–Ni(II) 25% electrodes can be appreciated from the top-view SEM images shown in Fig. 2. Both electrodes exhibit a planar surface and a structure composed of densely aggregated crystallites, which homogeneously cover the FTO underlayer with no evidence of phase segregation. However, a clear difference in the aggregates size is observed, with pure $CuWO_4$ presenting surface particles with size spanning from *ca.* 200 to *ca.* 250 nm (Fig. 2a) and $CuWO_4$-Ni(II) 25% showing much smaller, 70–100 nm-sized aggregates (Fig. 2b). Of course, a smaller surface particle size corresponds to a higher surface area of the photoactive material and thus a better contact with the electrolyte [25]. Higher surface areas have been also associated with a facilitated separation of the photogenerated charge carries [48]. Based on our previous work, the thickness of the photoelectrodes is estimated as *ca.* 80 nm [27].

The results of the EDX analyses performed on the two above-mentioned photoelectrodes are reported in Table 1. The elemental composition of the copper tungstate electrode perfectly matches its theoretical composition, with comparable atomic percent amounts of the two transition metals and thus a 1:1 Cu/W stoichiometry. The EDX results obtained with nickel-doped $CuWO_4$ confirm the presence of the Ni(II) ion into the copper tungstate structure and provide evidence of the effective doping on the Cu site only, with the

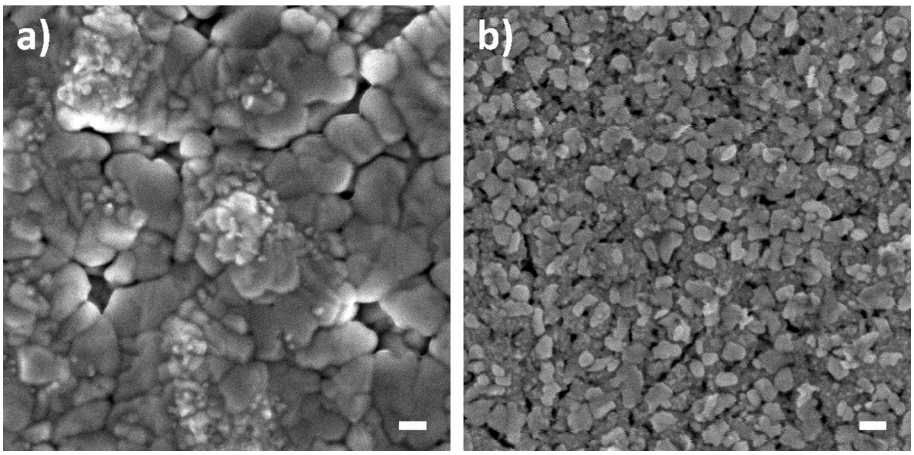

Fig. 2 Top-view images of **a** pure $CuWO_4$ and **b** $CuWO_4$–Ni(II) 25%. The scale bar is 100 nm

Table 1 Elemental composition of pure and $CuWO_4$–Ni(II) 25% photoanodes obtained through EDX analysis

$CuWO_4$ 0%		$CuWO_4$–Ni(II) 25%	
Element	Atom%	Element	Atom%
Cu	49.93	Cu	42.56
W	50.07	W	49.56
Ni	n.d	Ni	7.88

atomic percent amount of W being close to 50%, as in pure $CuWO_4$. The Ni/Cu ratio is 18.5%, slightly lower than the 25% nominal doping value. Thus, the Ni(II) content of the other dopant-containing photoelectrodes may be lower than the nominal values, possibly due to dopant loss during the synthesis and annealing process [49].

3.2 Photoelectrochemical tests

The linear sweep voltammetry (LSV) curves obtained by testing the photoanodes under simulated solar light are shown in Fig. 3. A common trend is observed under back- and front-side irradiation, with all electrodes with an Ni(II) content in the 0–10% range displaying a similar photocurrent onset at *ca.* 0.9 V vs. RHE, which is ~ 400 mV more positive than the conduction band edge of the material [25]. The photocurrent onset delay is larger in the case of $CuWO_4$ Ni 25%, which is evidence of a slower reaction kinetics [26].

The pure $CuWO_4$ electrode exhibits very modest performance in terms of photogenerated current, in line with the results reported for electrodes of similar thickness [50]. The photoanode containing 1% Ni(II) generates photocurrents very similar to pure $CuWO_4$ throughout the whole applied potential range, while the electrodes with higher nickel contents show different trends. In particular, $CuWO_4$–Ni(II) 10% is the best-performing photoanode, displaying higher

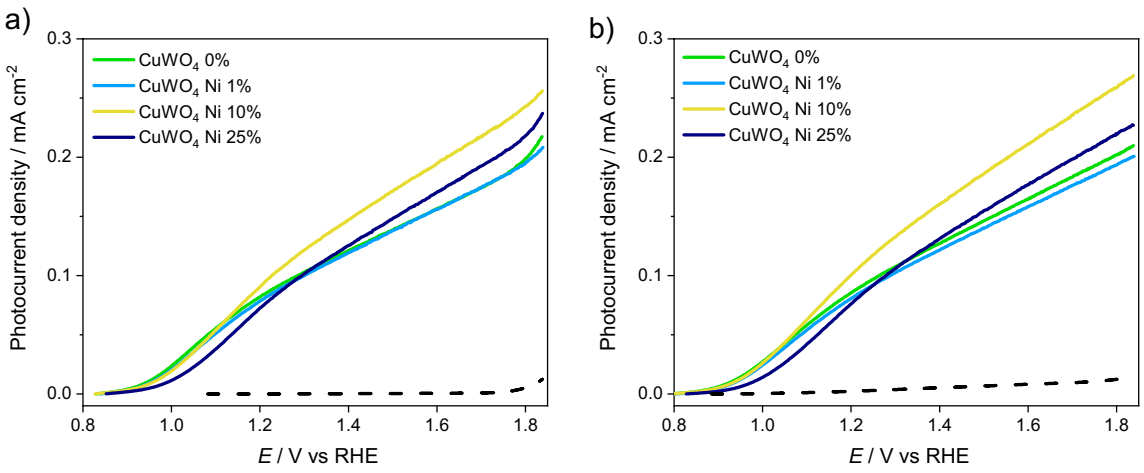

Fig. 3 Linear sweep voltammetry (LSV) curves recorded with pure and Ni(II)-doped $CuWO_4$ electrodes in KBi 0.1 M at pH 9 under **a** back- and **b** front-side irradiation. The dashed lines refer to dark scans

photocurrents already at low potentials (1.1 V vs. RHE) and generating the highest photocurrent at the water oxidation potential. Peculiar is the behavior of $CuWO_4$–Ni(II) 25%, which, although showing a slightly delayed photocurrent onset, exhibits a photocurrent higher compared to the pure and 1%-Ni(II) containing $CuWO_4$ electrodes at potentials higher than 1.4 V vs. RHE. Almost identical photocurrent intensities are generated by the photoanodes under the two irradiation configurations (see Fig. 3a vs. Figure 3b), which suggests similar transport properties of the photogenerated charge carriers, i.e., holes and electrons, within these very thin photoactive materials, when fully excited under solar simulated irradiation [51].

The photocurrent generated at 1.23 V vs. RHE under irradiation with light of different wavelength is shown in Fig. 4, reporting the incident photon to current efficiency (IPCE) and the internal quantum efficiency (IQE) vs. irradiation wavelength curves, recorded under both back- and front-side irradiation. The IPCE results (Fig. 4ab), referring to the efficiency in converting incident photons into current, are in full agreement with those obtained from LSV analyses (Fig. 3). $CuWO_4$–Ni(II) 10% confirms to be the best-performing photoanode, displaying the highest IPCE values throughout the whole investigated wavelength range, under both back-side (Fig. 4a) and front-side (Fig. 4b) irradiation. A clear photoactivity trend is difficult to identify among the other electrodes, all of them displaying very similar PEC performances.

The photoactivity of the electrodes, in terms of efficiency in converting absorbed photons in photocurrent, i.e., in terms of IQE values, allows a better evaluation of the intrinsic performance of photoactive materials. As shown in Fig. 4cd, also in this case pure copper tungstate and $CuWO_4$–Ni(II) 1% electrodes exhibit comparable performances, both of them reaching 6 and 8% IQE values under back- (Fig. 4c) and front-side (Fig. 4d) illumination, respectively. Electrodes with a higher nickel content show better photoactivity throughout the whole set of irradiation wavelengths, $CuWO_4$–Ni(II) 10 and 25% exhibiting *ca.* 20–25% IQE value increase compared to pure copper tungstate, without any shape modification of the IQE vs. wavelength curves. In particular, $CuWO_4$–Ni(II) 25% exhibits the highest IQE

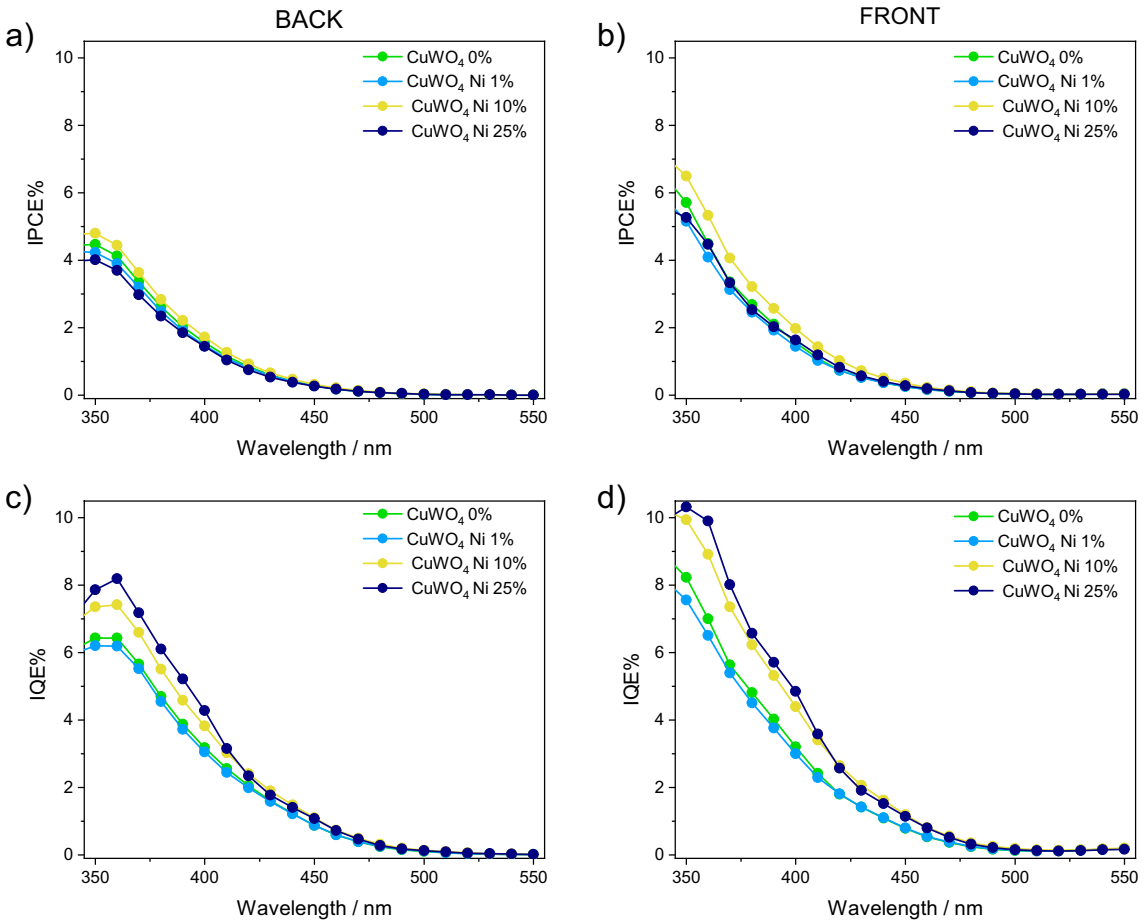

Fig. 4 **a, b** IPCE% and **c, d** IQE% of pure and Ni(II)-doped $CuWO_4$ photoanodes under **a, c** back- and **b, d** front-side monochromatic irradiation

curves, mainly because of its lower absorption spectrum (see Fig. 1a). We also observe that doping $CuWO_4$ with nickel does not result in an extended photoactivity to the visible region, eventually consequent to an alteration of the electronic structure of copper tungstate, as in the case of Mo for W substitution in $CuWO_4$ [37].

Both IPCE and IQE curves, recorded under low-intensity monochromatic irradiation, evidence a better performance of the electrodes under front- compared to back-side irradiation, pointing to a slightly better transport of electrons compared to holes in the here investigated $CuWO_4$-based thin films.

Finally, we compared the photocurrent density values recorded with the electrodes at 1.23 V vs. RHE in LSV analyses with the photocurrent density values obtained by integrating the product between the IPCE curves and the standard AM 1.5 G solar spectrum over the entire range of investigated wavelengths [52]. A good matching between the measured and integrated photocurrent values was obtained, as shown in Table 2. The slightly lower values calculated through integration are probably due to the much lower intensity of monochromatic light employed in IPCE analysis compared to the solar simulator light source employed in LSV analyses.

3.3 Charge injection and charge separation efficiencies

To ascertain the origin of the enhanced photoactivity of Ni(II)-doped copper tungstate, LSV analyses were conducted in the presence of a hole scavenger-containing electrolyte. In fact, by comparing the photocurrent densities obtained in the presence and in the absence of the hole scavenger, it is possible to calculate the charge separation efficiency of the photoactive material in the bulk and its charge injection efficiency at the interface with the electrolyte solution, as detailed below.

The maximum expected photocurrent density that can be generated by our electrodes, i.e., the absorption current density J_{abs}, which would be attained if all absorbed photons were converted into electricity, was calculated first, by integrating the product between the current theoretically generated by the standard AM 1.5 G solar spectrum emission and the absorption spectrum of the photoelectrodes in the 300–530 nm range (Fig. 1a). Usually, measured photocurrent densities (J_{PEC}) are much lower than J_{abs}, because only a fraction of the absorbed photons are successfully converted into current due to charge carrier recombination occurring at the surface and/or in the bulk of the photoactive material. J_{PEC} is thus related to J_{abs} according to the following equation [39, 53]:

$$J_{PEC} = J_{abs} \cdot \eta_{sep} \cdot \eta_{inj}, \quad (3)$$

where η_{sep} is the charge separation efficiency, i.e., the percent amount of photogenerated charge carriers that reach the semiconductor/electrolyte interface, whereas η_{inj} is the charge injection efficiency, i.e., the percent amount of the charge carriers that are injected into the electrolyte and take part in the water oxidation reaction. If PEC tests are conducted in the presence of a hole scavenger-containing electrolyte, η_{inj} can be assumed to be equal to 1 and η_{sep} can be easily calculated from Eq. (3), as $J_{PEC}/(J_{abs} \cdot \eta_{inj})$ is then calculated by dividing the J_{PEC} value measured for the water oxidation reaction in the absence of hole scavenger by the J_{PEC} value relative to the oxidation of the hole acceptor (when $\eta_{inj} = 1$), measured in the presence of the hole scavenger under identical conditions.

The charge injection and separation efficiencies, calculated by testing our photoanodes in a KBi 0.1 M pH 9 solution in the presence or absence of 0.1 M $NaNO_2$ as hole scavenger, are reported in Fig. 5. Sodium nitrite was chosen as suitable hole scavenger to be employed in contact with copper tungstate-based photoanodes after having tested a series of commonly used sacrificial species [37, 50]. Pure $CuWO_4$ displays the highest charge injection efficiency over the entire range of applied potentials and excellent surface properties, attaining almost quantitative surface water oxidation, in line with previous studies [50]. The introduction of nickel ions produces a decrease in the charge injection efficiency, η_{inj}. However, this effect is minimal in the case of the electrode containing 10% Cu(II), which shows an only slightly lower efficiency compared to the pure material, especially at potentials higher than 1.2 V vs. RHE. In any case, as shown in Table 3, the injection efficiency of these two electrodes is close to 90% at 1.23 V vs. RHE, which indicates an excellent water oxidation kinetics occurring at the electrode/electrolyte surface.

In contrast, the charge separation efficiencies of all photoanodes are quite low, below 5%, as shown in Fig. 5b, which indicates that the fast recombination of photogenerated electron/hole pairs in the bulk of the material is the major performance-limiting factor of our photoanodes. However, the introduction of nickel in the copper tungstate structure has

Table 2 Photocurrent density measured under back-side irradiation at 1.23 V vs. RHE in LSV plots and integrated photocurrent values calculated from IPCE analyses at the same applied potential for pure and Ni(II)-doped $CuWO_4$ photoanodes

	Measured photocurrent/mA cm^{-2}	Integrated photocurrent/mA cm^{-2}
$CuWO_4$ 0%	0.093	0.085
$CuWO_4$–Ni 1%	0.088	0.079
$CuWO_4$–Ni 10%	0.111	0.099
$CuWO_4$–Ni 25%	0.086	0.082

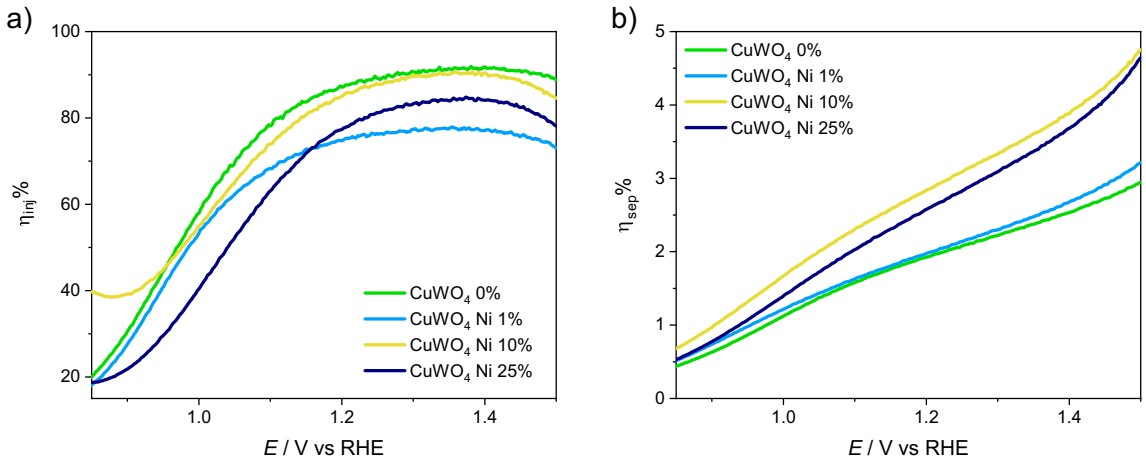

Fig. 5 **a** Charge injection and **b** charge separation efficiency values calculated for pure and Ni(II)-doped $CuWO_4$ photoanodes

Table 3 Maximum photocurrent density J_{abs}, charge injection efficiency η_{inj}% and charge separation efficiency η_{sep}% calculated at 1.23 V vs. RHE for pure and Ni(II)-doped $CuWO_4$ photoanodes

	J_{abs}/mA cm^{-2}	η_{inj}%	η_{sep}%
$CuWO_4$ 0%	3.23	88	2.03
$CuWO_4$–Ni 1%	3.17	76	2.07
$CuWO_4$–Ni 10%	2.79	87	2.99
$CuWO_4$–Ni 25%	2.68	80	2.73

a clear beneficial effect on the separation efficiency, since doped electrodes display higher or at least comparable η_{sep} values compared to pure $CuWO_4$ (see Table 3). $CuWO_4$ Ni 10% shows the highest separation efficiency, confirming to be the best-performing photoanode within the here investigated series.

4 Conclusions

Full lamp LSV analyses as well as IPCE and IQE analyses under monochromatic light evidence that 10 to 25% nickel doping of $CuWO_4$ increases the photoactivity of this material. While this would result from Ni^{2+} for Cu^{2+} lattice substitution for 10% nickel doping, the formation of $CuWO_4$/$NiWO_4$ heterojunction system appears plausible in the case of 25% nickel substitution. The superior performance of these electrodes can be attributed to the combined effects of the enhanced interface contact with the electrolyte solution, evidenced by morphological analysis, and of the remarkable increase in charge separation efficiency in the bulk of nickel-substituted $CuWO_4$, which is the bottleneck in the performance of tungstate photoanodes.

Funding Open access funding provided by Università degli Studi di Milano within the CRUI-CARE Agreement.

Declarations

Conflict of interest On behalf of all authors, the corresponding author states that there is no conflict of interest.

References

1. Dincer, I. (2000). Renewable energy and sustainable development: A crucial review. *Renewable and Sustainable Energy Reviews, 4*, 157–175.
2. Mathiesen, B. V., Lund, H., & Karlsson, K. (2011). 100% Renewable energy systems, climate mitigation and economic growth. *Applied Energy, 88*, 488–501.
3. Kim, J. H., Hansora, D., Sharma, P., Jang, J. W., & Lee, J. S. (2019). Toward practical solar hydrogen production-an artificial photosynthetic leaf-to-farm challenge. *Chemical Society Reviews, 48*, 1908–1971.
4. Gray, H. B. (2009). Powering the planet with solar fuel. *Nature Chemistry, 1*, 7.
5. Lewis, N. S. (2013). Toward cost-effective solar energy use. *Sustain Energy, 798*, 798–802.
6. N'Tsoukpoe, K. E., Liu, H., Le Pierrès, N., & Luo, L. (2009). A review on long-term sorption solar energy storage. *Renewable and Sustainable Energy Reviews, 13*, 2385–2396.

7. Tachibana, Y., Vayssieres, L., & Durrant, J. R. (2012). Artificial photosynthesis for solar water-splitting. *Nature Photonics, 6*, 511–518.
8. Hisatomi, T., Kubota, J., & Domen, K. (2014). Recent advances in semiconductors for photocatalytic and photoelectrochemical water splitting. *Chemical Society Reviews, 43*, 7520–7535.
9. Walter, M. G., Warren, E. L., McKone, J. R., Boettcher, S. W., Mi, Q., Santori, E. A., & Lewis, N. S. (2010). Solar water splitting cells. *Chemical Reviews, 110*, 6446–6473.
10. Jaramillo, T. F., Deutsch, T. G., Gaillard, N., & Dinh, H. N. (2010). Accelerating materials development for photoelectrochemical hydrogen production: Standards for methods, definitions, and reporting protocols. *Journal of Materials Research, 25*, 3–16.
11. Sivula, K., & van de Krol, R. (2016). Semiconducting materials for photoelectrochemical energy conversion. *Nature Reviews Materials, 1*, 15010.
12. Lee, D. K., Lee, D., Lumley, M. A., & Choi, K.-S. (2019). Progress on ternary oxide-based photoanodes for use in photoelectrochemical cells for solar water splitting. *Chemical Society Reviews, 48*, 2126–2157.
13. Tang, Y., Rong, N., Liu, F., Chu, M., Dong, H., Zhang, Y., & Xiao, P. (2016). Enhancement of the photoelectrochemical performance of $CuWO_4$ films for water splitting by hydrogen treatment. *Applied Surface Science, 361*, 133–140.
14. Thang, H. V., Albanese, E., & Pacchioni, G. (2019). Electronic structure of CuWO4: Dielectric-dependent, self-consistent hybrid functional study of a Mott-Hubbard type insulator. *Journal of Physics: Condensed Matter, 31*, 145503.
15. Jeong, H. W., Jeon, T. H., Jang, J. S., Choi, W., & Park, H. (2013). Strategic modification of $BiVO_4$ for improving photoelectrochemical water oxidation performance. *Journal of Physical Chemistry C, 117*, 9104–9112.
16. Wang, Z., Huang, X., & Wang, X. (2019). Recent progresses in the design of $BiVO_4$-based photocatalysts for efficient solar water splitting. *Catalysis Today, 335*, 31–38.
17. Tayebi, M., & Lee, B. K. (2019). Recent advances in $BiVO_4$ semiconductor materials for hydrogen production using photoelectrochemical water splitting. *Renewable and Sustainable Energy Reviews, 111*, 332–343.
18. Kim, J. H., Jang, Y. J., Kim, J. H., Jang, J. W., Choi, S. H., & Lee, J. S. (2015). Defective $ZnFe_2O_4$ nanorods with oxygen vacancy for photoelectrochemical water splitting. *Nanoscale, 7*, 19144–19151.
19. Guijarro, N., Bornoz, P., Prévot, M. S., Yu, X., Zhu, X., Johnson, M., Jeanbourquin, X., Le Formal, F., & Sivula, K. (2018). Evaluating spinel ferrites MFe_2O_4 (M = Cu, Mg, Zn) as photoanodes for solar water oxidation: Prospects and limitations. *Sustain Energy Fuels, 2*, 103–117.
20. Yourey, J. E., & Bartlett, B. M. (2011). Electrochemical deposition and photoelectrochemistry of $CuWO_4$, a promising photoanode for water oxidation. *Journal of Materials Chemistry, 21*, 7651–7660.
21. Guo, W., Duan, Z., Mabayoje, O., Chemelewski, W. D., Xiao, P., Henkelman, G., Zhang, Y., & Mullins, C. B. (2016). Improved charge carrier transport of hydrogen-treated copper tungstate: Photoelectrochemical and computational study. *Journal of the Electrochemical Society, 163*, H970–H975.
22. Liu, Y., Xia, M., Yao, L., Mensi, M., Ren, D., Grätzel, M., Sivula, K., & Guijarro, N. (2021). Spectroelectrochemical and chemical evidence of surface passivation at zinc ferrite ($ZnFe_2O_4$) photoanodes for solar water oxidation. *Advanced Functional Materials, 31*, 2010081.
23. Yourey, J. E., Pyper, K. J., Kurtz, J. B., & Bartlett, B. M. (2013). Chemical stability of $CuWO_4$ for photoelectrochemical water oxidation. *Journal of Physical Chemistry C, 117*, 8708–8718.
24. Lhermitte, C. R., & Bartlett, B. M. (2016). Advancing the chemistry of $CuWO_4$ for photoelectrochemical water oxidation. *Accounts of Chemical Research, 49*, 1121–1129.
25. Hill, J. C., & Choi, K.-S. (2013). Synthesis and characterization of high surface area $CuWO_4$ and Bi_2WO_6 electrodes for use as photoanodes for solar water oxidation. *Journal of Materials Chemistry A, 1*, 5006–5014.
26. Pyper, K. J., Yourey, J. E., & Bartlett, B. M. (2013). Reactivity of $CuWO_4$ in photoelectrochemical water oxidation is dictated by a midgap electronic state. *Journal of Physical Chemistry C, 117*, 24726–24732.
27. Grigioni, I., Polo, A., Dozzi, M. V., Ganzer, L., Bozzini, B., Cerullo, G., & Selli, E. (2021). Ultrafast charge carrier dynamics in $CuWO_4$ photoanodes. *Journal of Physical Chemistry C, 125*, 5692–5699.
28. Wu, Z., Zhao, Z., Cheung, G., Doughty, R. M., Ballestas-Barrientos, A. R., Hirmez, B., Han, R., Maschmeyer, T., & Osterloh, F. E. (2018). Role of surface states in photocatalytic oxygen evolution with $CuWO_4$ particles. *Journal of the Electrochemical Society, 166*, H3014–H3019.
29. Klahr, B., Gimenez, S., Fabregat-Santiago, F., Hamann, T., & Bisquert, J. (2012). Water oxidation at hematite photoelectrodes: The role of surface states. *Journal of the American Chemical Society, 134*, 4294–4302.
30. Wang, D., Bassi, P., Qi, H., Zhao, X., Gurudayal, W., & L., Xu, R., Sritharan, T. & Chen, Z. (2016). Improved charge separation in WO_3/$CuWO_4$ composite photoanodes for photoelectrochemical water oxidation. *Materials (Basel), 9*, 348.
31. Pilli, S. K., Deutsch, T. G., Furtak, T. E., Brown, L. D., Turner, J. A., & Herring, A. M. (2013). $BiVO_4$/$CuWO_4$ heterojunction photoanodes for efficient solar driven water oxidation. *Physical Chemistry Chemical Physics: PCCP, 15*, 3273–3278.
32. Rodríguez-Gutiérrez, I., Djatoubai, E., Rodríguez-Pérez, M., Su, J., Rodríguez-Gattorno, G., Vayssieres, L., & Oskam, G. (2019). Photoelectrochemical water oxidation at FTO|WO_3@$CuWO_4$ and FTO|WO_3 @$CuWO_4$|$BiVO_4$ heterojunction systems: An IMPS analysis. *Electrochimica Acta, 308*, 317–327.
33. Hamann, T. W., Shadabipour, P., & Raithel, A. L. (2020). Charge-carrier dynamics at the $CuWO_4$/electrocatalyst interface for photoelectrochemical water oxidation. *ACS Applied Materials & Interfaces, 12*, 50592–50599.
34. Nam, K. M., Cheon, E. A., Shin, W. J., & Bard, A. J. (2015). Improved photoelectrochemical water oxidation by the WO_3/$CuWO_4$ composite with a manganese phosphate electrocatalyst. *Langmuir, 31*, 10897–10903.
35. Bohra, D., & Smith, W. A. (2015). Improved charge separation via Fe-doping of copper tungstate photoanodes. *Physical Chemistry Chemical Physics: PCCP, 17*, 9857–9866.
36. Li, C., & Diao, P. (2020). Fluorine doped copper tungsten nanoflakes with enhanced charge separation for efficient photoelectrochemical water oxidation. *Electrochimica Acta, 352*, 136471–136479.
37. Polo, A., Nomellini, C., Grigioni, I., Dozzi, M. V., & Selli, E. (2020). Effective visible light exploitation by copper Molybdotungstate photoanodes. *ACS Applied Energy Materials, 3*, 6956–6964.
38. Hill, J. C., Ping, Y., Galli, G. A., & Choi, K.-S. (2013). Synthesis, photoelectrochemical properties, and first principles study of n-type $CuW_{1-x}Mo_xO_4$ electrodes showing enhanced visible light absorption. *Energy & Environmental Science, 6*, 2440–2446.
39. Ye, W., Chen, F., Zhao, F., Han, N., & Li, Y. (2016). $CuWO_4$ nanoflake array-based single-junction and heterojunction photoanodes for photoelectrochemical water oxidation. *ACS Applied Materials & Interfaces, 8*, 9211–9217.
40. Hu, D., Diao, P., Xu, D., Xia, M., Gu, Y., Wu, Q., Li, C., & Yang, S. (2016). Copper (II) tungstate nanoflake array films: Sacrificial

template synthesis, hydrogen treatment, and their application as photoanodes in solar water splitting. *Nanoscale, 3*, 5892–5901.
41. Fan, L., Sunarso, J., Zhang, X., Xiong, X., He, L., Luo, L., Wang, F., Fan, Z., Wu, C., Han, D., Wong, N. H., Wang, Y., Chen, G., & Chen, W. (2022). Regulating the hole transfer from $CuWO_4$ photoanode to $NiWO_4$ electrocatalyst for enhanced water oxidation performance. *International Journal of Hydrogen Energy, 47*, 20153–20165.
42. Basyach, P., Guha, A. K., Borthakur, S., Kalita, L., Chetia, P., Sonowal, K., & Saikia, L. (2020). Efficient hydroxylation of benzene to phenol by H_2O_2 using Ni-doped $CuWO_4$ on carbon nitride as a catalyst under solar irradiation and its structure-activity correlation. *Journal of Materials Chemistry A, 8*, 12774–12789.
43. Meng, S., Li, L., Xi, H., Yang, J., Xiao, T., Zuo, R., Xu, X., Lei, Z., Yang, Z., & Xue, Q. (2022). Visible-light photocatalytic and photo-bactericidal activity of Ni-$CuWO_4$/$OTiO_2$ composite. *Chinese Journal of Chemistry, 40*, 2701–2711.
44. Liao, J., Shao, Y., Feng, Y., Zhang, J., Song, C., Zeng, W., Tang, J., Dong, H., Liu, Q., & Li, H. (2023). Interfacial charge transfer induced dual-active-sites of heterostructured $Cu_{0.8}Ni_{0.2}WO_4$ nanoparticles in ammonia borane methanolysis for fast hydrogen production. *Applied Catalysis B: Environmental, 320*, 121973.
45. Dey, S., Ricciardo, R. A., Cuthbert, H. L., & Woodward, P. M. (2014). Metal-to-metal charge transfer in AWO_4 (A = Mg, Mn Co, Ni, Cu, or Zn) compounds with the wolframite structure. *Inorganic Chemistry, 53*, 4394–4399.
46. Liu, Y., Chen, J., Zhu, X., Qiu, H., Wang, K., Li, W., Cao, S., Zhang, T., Cai, Y., Wu, Q., & Li, J. (2022). Effects of operating temperature on photoelectrochemical performance of $CuWO_4$ film photoanode. *Journal of Electroanalytical Chemistry, 924*, 116859.
47. Chen, L., Li, W., Qiu, W., He, G., Wang, K., Liu, Y., Wu, Q., & Li, J. (2022). Oriented $CuWO_4$ films for improved photoelectrochemical water splitting. *ACS Applied Materials & Interfaces, 14*, 47737–47746.
48. Klahr, B., Giménez, S., Fabregat-Santiago, F., Bisquert, J., & Hamann, T. W. (2012). Photoelectrochemical and impedance spectroscopic investigation of water oxidation with 'co-Pi'-coated hematite electrodes. *Journal of the American Chemical Society, 134*, 16693–16700.
49. Polo, A., Grigioni, I., Magni, M., Facibeni, A., Dozzi, M. V., & Selli, E. (2021). Unravelling the bulk and interfacial charge transfer effects of molybdenum doping in $BiVO_4$ photoanodes. *Applied Surface Science, 556*, 149759.
50. Gao, Y., & Hamann, T. W. (2017). Quantitative hole collection for photoelectrochemical water oxidation with $CuWO_4$. *Chemical Communications, 53*, 1285–1288.
51. Liang, Y., Tsubota, T., Mooij, L. P. A., & Van De Krol, R. (2011). Highly improved quantum efficiencies for thin film $BiVO_4$ photoanodes. *Journal of Physical Chemistry C, 115*, 17594–17598.
52. Christians, J. A., Manser, J. S., & Kamat, P. V. (2015). Best practices in perovskite solar cell efficiency measurements. Avoiding the error of making bad cells look good. *Journal of Physical Chemistry Letters, 6*, 852–857.
53. Govindaraju, G. V., Wheeler, G. P., Lee, D., & Choi, K.-S. (2017). Methods for electrochemical synthesis and photoelectrochemical characterization for photoelectrodes. *Chemistry of Materials, 29*, 355–370.